International Journal of Chemical, Materials and Biomolecular Sciences
ISSN: 2415-6620
Vol:9, No:7, 2015

Speciation of Iron (III) Oxide Nanoparticles and Other Paramagnetic Intermediates during High-Temperature Oxidative Pyrolysis of 1-Methylnaphthalene

Michael P. Herring, Lavrent Khachatryan, Barry Dellinger

Abstract**—**Low Temperature Matrix Isolation - Electron Paramagnetic Resonance (LTMI-EPR) Spectroscopy was utilized to identify the species of iron oxide nanoparticles generated during the oxidative pyrolysis of 1-methylnaphthalene (1-MN). The otherwise gas-phase reactions of 1--MN were impacted by a polypropylenimine tetra-hexacontaamine dendrimer complexed with iron (III) nitrate nonahydrate diluted in air under atmospheric conditions. The EPR fine structure of Fe $(III)_2O_3$ nanoparticles clusters, characterized by g-factors of 2.00, 2.28, 3.76 and 4.37 were detected on a cold finger maintained at 77 K after accumulation over a multitude of experiments. Additionally, a high valence Fe (IV) paramagnetic intermediate and superoxide anion-radicals, $O_2^{\bullet-}$ adsorbed on nanoparticle surfaces in the form of Fe (IV) --- $O_2^{\bullet-}$ were detected from the quenching area of Zone 1 in the gas-phase.

Keywords**—**Cryogenic trapping, EPFRs, dendrimer, Fe_2O_3 doped silica, soot.

I. Introduction

THE contribution of redox-active transition metals and adsorbed organic species to the molecular growth of soot was investigated in recent studies within a high-temperature flow reactor where iron-oxide nanoparticles were introduced to a high sooting 1-methylnapthalene (1-MN) fuel [1].

The contribution of redox-active transition metals and adsorbed organic species to the molecular growth of soot was investigated in recent studies within a high-temperature flow reactor where iron-oxide nanoparticles were introduced to a high sooting 1-methylnapthalene (1-MN) fuel [1].

Increased PAH formation, soot number density, soot mass yield, and soot radical intensity were observed as a result of iron oxide nanoparticles introduction prior to soot inception.

The observation of enhanced PAH and soot formation as well as increased sooting tendency have been reported in a number of other studies when ferrocene was doped to premixed flames [2], [3]. Conversely, enhanced soot oxidation rates and reduced mass yields have also been reported upon the addition of ferrocene and iron pentacarbonyl to flames [4]-[6].

Although both promotion and inhibition of soot were concluded, addition of ferrocene or iron pentacarbonyl to flames resulted in the formation of condensation nuclei prior to soot inception [3], [7], [8]. These nuclei provided a surface for condensation of carbonaceous matter [8], which may have initiated soot surface growth [3].

The prospective for metal oxides to actively participate in the stabilization of organic precursors and the growth to larger species is further supported by pollutant formation on redox-active transition metals. Redox-active transition metal oxide nanoparticles, such as copper and iron oxides, have been identified as active sites for the formation and stabilization of environmentally persistent free radicals (EPFRs) [9], [10]. In thermal and combustion processes, EPFRs form on the surfaces of transition metal-containing particles by chemisorption of a molecular precursor, e.g. hydroquinone, catechol, chlorinated phenols, and chlorinated benzenes, to the metal oxide surface [10], [11]. The organic radical is formed when an electron is transferred from the organic precursor to the metal oxide species. This radical is both resistant to oxidation and stabilized by the metal oxide surface, such that it can persist in the environment for days [11]. However, molecular growth can proceed when these radicals are at higher concentrations and elevated temperatures [11]. EPFRs can self-react or "dimerize" to form pollutants such as polychlorinated dibenzo-p-dioxins and dibenzofurans or "oligomerize" to form small polycyclic aromatic hydrocarbons (PAHs) [12], [13].

Key questions in this mechanism of molecular growth include: what metal species are initially present and how are the nanoparticles transformed as result of molecular growth? It is additionally complicated if the metal containing nanoparticles are present **in** the gas-phase are more difficult to study because of their small particle size and low concentration.

Low Temperature Matrix Isolation - Electron Paramagnetic Resonance (LTMI-EPR) [11], [14] is capable of identifying intermediate paramagnetic species, including organic free radicals and paramagnetic metal oxides. LTMI-EPR was utilized to examine the species present during the oxidative pyrolysis of 1-MN diluted in air in the presence of iron oxide nanoparticles within the high temperature flow reactor maintained at atmospheric conditions.

II. Experimental

EPR Spectroscopy was utilized to identify the species and oxidation state of the iron oxide nanoparticles generated within a dual-zone, high-temperature flow reactor prior to and

Michael Herring is with the LSU, Department of Chemistry, Baton Rouge, LA, 70803 USA (e-mail: mherri7@lsu.edu).
Lavrent Khachatryan is with the LSU, Department of Chemistry, Baton Rouge, LA, 70803 USA (phone: 225 578 4417; e-mail: lkhach1@lsu.edu)
Barry Dellinger is with the LSU, Department of Chemistry, Baton Rouge, LA, 70803 USA (e-mail: barryd@lsu.edu).

following the oxidative pyrolysis of 1-MN under atmospheric conditions, in which soot formation was enhanced by the addition of iron-oxide nanoparticles [1], [15].

A. Materials

$Fe(NO_3)_3*9H_2O$ (99.99%, trace metal basis), CH_3OH (ACS reagent grade), 1- methylnaphtalene (1-MN) (95% purityM56808-100G) was obtained from Sigma-Aldrich, Cab-O-Sil^{TM} from Cabot (EH-5, 99+%). Dendrimer - generation 4 polypropylenimine tetra-hexacontaamine dendrimer, (Dendrimer DAB - Am_{32}) with 32 amine functional groups was obtained from SYMO-Chem (cf. Fig. 6, Appendix), $^{57}Fe_2O_3$ (96.64%) from Cambridge Isotope laboratories Inc.

The flow of the gasses was controlled by McMillan Mass Flow Controllers; injection of reagents into reaction zone by KD Scientific Model 100 syringe pumps.

B. Generation of Iron Oxide Nanoparticles and Soot

The details of the dual zone reactor are described in detail elsewhere [1]. Briefly, a two-zone, fused silica, and heterogeneous-flow reactor system was utilized to generate soot from the oxidative pyrolysis of 1-MN (diluted in air) under atmospheric conditions in the presence of iron oxide nanoparticles, Fig. 1, Zone 1. Zone 1 (a 33 cm fused silica tube, O.D = 2.5cm) generated the metal oxide nanoparticles *in situ* from the oxidation of a polypropylenimine tetra-hexacontaamine dendrimer (Fig. 6) complexed with iron (III) nitrate nonahydrate under stoichiometric quantities of air diluted in nitrogen. A methanolic solution of the dendrimer-metal complex was delivered at 85μL/h with a syringe pump into the reactor maintained at 700˚C and 1 atm. The gas-phase residence time in Zone 1 was maintained at 60 s. Upon oxidation of the dendrimer, ~5 nm iron oxide nanoparticles were formed and were continually introduced into Zone 2 of the reactor (a 51 cm fused silica tube, (O.D = 0.6 cm) to a high sooting 1-MN fuel at a fuel/air equivalence ratio (φ) of 2.5 [1].

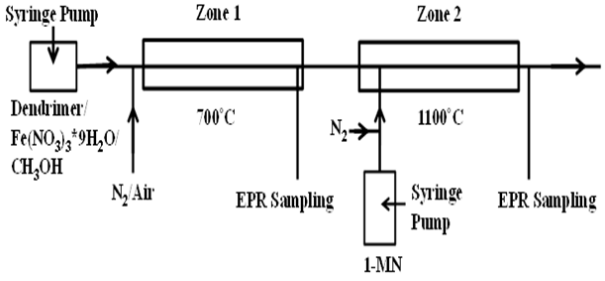

Fig. 1 Schematic of experimental dual zone reactor

The nanoparticles size was determined through TEM analysis to be ~5 nm and was confirmed with a condensation particle counter (DMA Model 3085 equipped with UCPC). The gas phase calculated concentration of iron oxide nanoparticles was in ppm level in Zone 2, Fig. 1. Zone 2 of the dual zone reactor was maintained at 1100˚C and 1 atm. with a gas-phase residence time of 1.0 s.

C. Gas Phase Sampling

A small quantity of effluent was drawn through a sampling orifice (i.d. ~ 100μM) located at the end of either Zone 1 or Zone 2 of the dual zone reactor (Fig. 1) and condensed on a Dewar cold finger maintained at 77 K using liquid nitrogen. This gas-phase sampling technique has been extensively described in the literature [11]. The Dewar was positioned in the cavity of the EPR spectrometer for *in-situ* measurements. A rotary pump was used to maintain the pressure at < 0.5 torr to transport the by-products to the cold finger without disturbing the chemistry in the flow reactor. The expansion of the gas-mixture in the orifice region resulted in a rapid decrease of temperature, which further suppressed chemical and physical changes. Carbon dioxide was introduced as a supporting matrix at 77 K to optimize the condensation of products (as well as stable radicals) and increase the resolution of the EPR spectra of cryogenically trapped radicals.

D. EPR Measurements

EPR spectra were recorded using a Bruker EMX-20/2.7 EPR spectrometer (X-band) with dual cavities, modulation and microwave frequencies of 100 kHz and 9.516 GHz, respectively. Typical parameters were: sweep width of 5000 G, EPR microwave power of 10 mW (and less) modulation amplitude of 2 G, time constant of 40.96 ms, and sweep time of 167.77s. Values of the g-tensor were calculated using Bruker's WIN-EPR SimFonia 2.3 program, which allowed control of the Bruker EPR spectrometer, data-acquisition, automation routines, tuning, and calibration programs on a Windows-based PC. The exact g-factors for key spectra were determined by comparison with a 2,2-diphenyl-1-picrylhydrazyl (DPPH) standard. EPR measurements for the standards and 0.5-5 % $Fe(III)_2O_3$/silica model systems were made in a 4 mm quartz EPR tube at room temperature and 77K.

E. Generation of Impregnated $Fe(III)_2O_3$ on Silica

For use as standards, $Fe(III)_2O_3$, nanoclusters of 0.5-5 % $Fe(III)_2O_3$/silica were prepared by impregnation of silica powder (Cab-O-Sil^{TM}) with an appropriate solution of iron(III)nitrate nonahydrate tethered with polypropylenimine tetra-hexacontaamine dendrimer. The solution was mixed for 24 hrs, and then the methanol solvent was removed. The powder was dried at 100˚C for 24 hrs and calcined at 450°C for 12 hrs [9], [10]. The $Fe(III)_2O_3$ impregnated silica was then ground and sieved to a 230 mesh size (63 μm).

F. Preparation of ^{57}Fe labeled Iron (III) Nitrate Nonahydrate

Iron (III) nitrate nonahydrate doped by ^{57}Fe was used in some experiments. The initial reagent solutions of $^{56}Fe(NO_3)_3$ and $^{57}Fe(NO_3)_3$ in water were prepared from $^{56}Fe_2O_3$ and $^{57}Fe_2O_3$, respectively in a substoichiometric quantity of 30% HNO_3 in water to ensure no excess HNO_3. The excess amount of $^{56}Fe_2O_3$ or $^{57}Fe_2O_3$ was then removed through centrifugation and subsequent decantation. Iron (III) nitrate nonahydrate synthesized from $^{56}Fe_2O_3$, served as a control to the

experiment to ensure the synthesis route resulted in the experimental spectra observed from other precursors.

III. Results and Discussions

One of the advantages of LTMI-EPR technique is the accumulation of intermediate labile species (radicals) from the gas phase on the cold finger at 77 K for long periods (lasting some time hours) until quantities are obtained that are detectable by EPR. The small sampling orifice and long accumulation period result in an improved EPR signal/noise ratio that is optimal for identification of species. This also minimizes the possibility of concentration broadening especially in the cases of transition metals. When metallic species contain one or more unpaired d electrons, EPR spectroscopy can provide a description of the metals local chemical environment and binding properties [16].

For instance, Fe(III) ions, with an electronic configuration $[Ar]3d^5$ and s= 5/2, are well suited for EPR analysis because the ground state of the paramagnetic ions split into a number of components resulting in a fine structured EPR spectrum [17]. However, the EPR spectra of metal species at elevated concentrations are often characterized by broadened absorption lines [18]. These broad features are sometimes observed for iron species and make it difficult to make exact assignments of the species present in the system with EPR spectroscopy. For instance, at elevated concentrations $Fe(III)_2O_3$, FeO(OH), and Fe_3O_4 exhibit the same g-factor of 2.00 and overall line shape [17], [19]-[21]. This results in the assignment of these large broadened absorption lines as an agglomeration of paramagnetic centers but provides little or no detail on the speciation of iron within the system (Fig. 7, Appendix).

A. EPR Sampling from Zone 2

Introduction of iron oxide nanoparticles into Zone 2 of the dual-zone reactor (from Zone 1, Fig. 1) in the presence of 1-MN resulted in enhanced soot formation and radical formation identified through the detection of a unique organic radical signal represented in Fig. 2, inset. The identification of this superimposed EPR signal as a mixture of organic radicals (carbon and oxygen-centered) and soot has been reported elsewhere [15]. The carbon-centered radicals were identified as a mixture of the resonance-stabilized indenyl, cyclopentadienyl, and naphthalene 1-methylene radicals and that formation of these radical species was promoted by the addition of iron oxide nanoparticles.

As an unexpected consequence of studying soot, paramagnetic species began accumulating on the Dewar cold-finger over the time period of the experiments and remained on the finger of Dewar after each experiment, Fig. 2.

The original Dewar EPR signal (Fig. 2 **a**) exhibited spectral features consistent with Fe(III) in high-quality silica glass [22], [23]. After sampling/collection over a four month period (Fig. 2 **b-d)** spectrum **(d)** was compared to a standard of 50 nm $Fe(III)_2O_3$ nanoparticles (Fig. 2 **e**) and was found to exhibit the same spectral features.

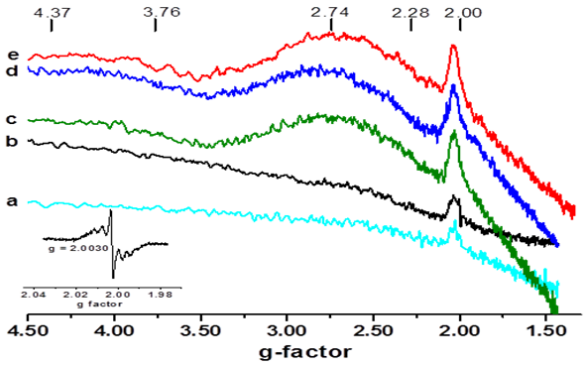

Fig. 2 Comparison of EPR signal of the Dewar cold-finger as a function of accumulation time: spectrum (a) (initial, without accumulation), spectrum (b) (1 month accumulation), spectrum (c) (3 months accumulation), spectrum (d) (4 months accumulation) and spectrum (e) (50nm Fe_2O_3 nanoparticle standard)

A five-fold increase in the signal intensity at g~2.00 resulted from condensation of products over a four month period of experimentation. Although there was an observed increase in signal intensity at g~2.00 and g = 2.28, the peaks at g = 4.48 and 3.76 remained very weak (for these peaks ref. Fig. 8 in large range of g-factors, Appendix).

Spectral assignment of g-factors are reported in the literature for Fe(III) in silicate glass [18], [22], [24]-[28]. For some experiments, the EPR spectrum of Fe(III) in a disordered system consisted mainly of lines at g ~ 4.30 and g ~ 2.00 [18], [24]. Multiple interpretations of these g-factors have been proposed. The g ~ 4.30 resonance has been assigned to both tetra- or octo-coordinated Fe(III) [25], [26], and rhombic distortion of both tetrahedral and octahedral Fe(III) [27], [28]. The g = 2.00 resonance has been interpreted as due to either octa - coordinated Fe(III) [25], [26] or clusters of Fe(III) ions coupled by strong spin-spin interaction [28]. The broad signals centered at g = 2.28 were attributed to paramagnetic species in the form of aggregates [17], [29]. The appearance of the EPR line at g = 3.76 is in good agreement with the theoretical possibility of obtaining isotropic g-factors of 2,00 3.30 and 4.30 for $3d^5$ ions [30], [31].

B. Iron Oxide Model System

Usually iron species exhibit large broad featureless spectra at elevated concentrations, Fig. 6.

The spectral features, associated with relatively low concentrations of iron oxides, observed at characteristic g-factors of 2.00, 2.28, 3.76 and 4.37 are often not resolved in a large magnetic field of up to 6000 G at high concentrations (cf Fig. 6).

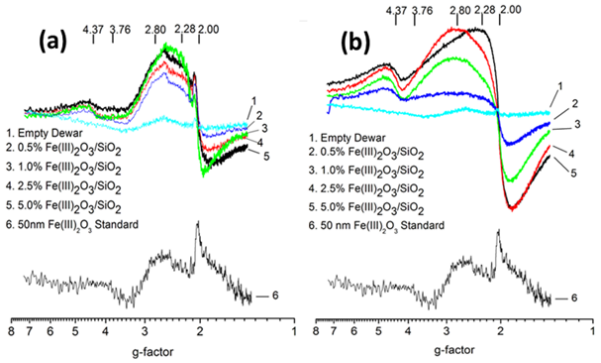

Fig. 3 (a) EPR spectra of 3 mg of $Fe(III)_2O_3$ doped silica particles (0.5-5.0 % $Fe(III)_2O_3$, w/w) measured at room temperature for comparison with a 50 nm $Fe(III)_2O_3$ standard. **(b)** EPR spectra of 50 mg of $Fe(III)_2O_3$ doped silica particles (0.5-5.0 % $Fe(III)_2O_3$, w/w) measured at room temperature for comparison with 50 nm $Fe(III)_2O_3$ standard

In an attempt to minimize spectral features lost from concentration broadening, silica was impregnated with 0.5-5.0 % $Fe(III)_2O_3$ (w/w), to control the concentration and size of $Fe(III)_2O_3$ clusters. This method of preparation resulted in the formation of $Fe(III)_2O_3$ nanoclusters impregnated in silica which have been extensively studied [10], [32], [33]. The EPR spectra of 3 mg samples of $Fe(III)_2O_3$ impregnated silica are presented in Fig. 3 **a**, spectra 2-5. With the exception of the weak line at g ~3.76, these EPR spectra have all of the features associated with $Fe(III)_2O_3$ doped silica previously reported in the literature. Increasing the quantity of $Fe(III)_2O_3$ from 3 mg to 50 mg resulted in concentration broadening, which caused spectral lines to merge (c.f. Fig. 3 **b** spectra **2-5)** and complete disappearance of the line centered at g = 3.76. Comparison of the EPR signal as the mass was increased from 3 to 50 mg (Fig. 3**, a** and **b**) clearly demonstrated reduction in the sensitivity of the fine structure for transition metal ions as a function of mass. Instead of two separated peaks centered at g~2.00 and g~2.28, Fig. 3 **a**, spectra **2-5**, broadening caused those peaks to merge and appear as a broad peak centered at g~2.01 (not labeled) with ΔH_{p-p} = 870 G (Fig. 3 **b**, spectra **2-5**). These line-widths matched the broad signals reported in the literature [17], [29] and were attributed to paramagnetic species in the form of aggregates. Nanogram quantities of 50 nm $Fe(III)_2O_3$ nanoparticles exhibited features also observed in 3 mg samples of $Fe(III)_2O_3$ doped silica (Fig. 3 **a**), providing further confirmation of the presence of $Fe(III)_2O_3$. Concentration broadening was minimized by the distribution of $Fe(III)_2O_3$ in silica and resulted in spectral features that could be utilized to elucidate the speciation of iron. These spectral features observed in $Fe(III)_2O_3$ doped silica were utilized to clarify the speciation of iron generated in Zone 1 and subsequent changes resulting from the addition of 1-MN in Zone 2, Fig. 1. Thus, the peak at g = 3.76 is characteristic for very small amounts of iron i.e. iron clusters documented here, Fig. 2 **d** and in standard, Fig. 2 **e** or Fig. 3, line 6.

C. EPR Sampling from Zone 1

The oxidation of polypropylenimine tetra-hexacontaamine dendrimer complexed with iron (III) nitrate nonahydrate primarily resulted in the formation of $Fe(III)_2O_3$ nanoparticles and were detected from the outlet of Zone 2 (Fig. 1) using the LTMI-EPR technique described above. The intermediate species formed in Zone 1 of the reactor were directly identified through sampling flow from the Zone 1 reactor and accumulation on the cold finger, Fig. 1. The Zone 1 reactor was separated from the Zone 2 reactor and the probe was placed at the exit of the reactor. It is important to note the Dewar already contained $Fe(III)_2O_3$ nanoparticles accumulated from previous experiments on the finger, Fig. 4, peak (**a**).

The EPR spectra of the cryogenically trapped new intermediates overlaid on the EPR spectrum of the $Fe(III)_2O_3$ nanoparticles is referred to as the triplet EPR spectrum and is presented in Fig. 4 **b** and in an expanded version as an inset spectrum. The initial background spectrum of Dewar has also been presented for comparison, Fig. 4**,** black line.

The spectral features observed with g-factors of 2.03, 2.00, and 1.96 have not been reported in the literature for the gas-phase synthesis of iron oxide nanoparticles. Control experiments, described below, confirmed these observed spectral features did not result from the dendrimeric backbone or the methanolic solution.

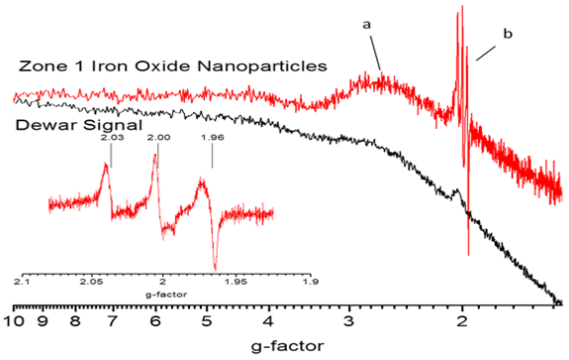

Fig. 4 EPR of iron oxide nanoparticles generated from the oxidation of polypropylenimine tetra-hexacontaamine dendrimer complexed with iron (III) nitrate nonahydrate, red line (a) and overlaid new intermediate 3 lines spectrum (b). Inset – expanded spectrum of (b) in 300 G window

Gradual warming of the Dewar cold-finger resulted in the disappearance of the triplet spectrum, indicating these species were a highly unstable paramagnetic intermediate and is not saturated readily at high microwave power (64 mW) at 77K. This signal was also not obtainable in the absence of oxygen. Multiple experiments were then performed to identify the origin of the triplet, highly anisotropic spectra.

D. $Fe(III)_2O_3$ Nanoparticle Generation from Various Precursors

Iron oxide nanoparticles were generated from various iron precursors to confirm the triplet spectra observed at g-factors of 2.03, 2.00, and 1.96 resulted from the presence of iron

within the system and were not an artifact of the sampling procedure, dendrimer structure, or methanol solvent. Nanoparticles were generated from polypropylenimine tetra-hexacontaamine dendrimers (G3-G5 generation) complexed with iron (III) nitrate nonahydrate (c.f. Fig. 9, Appendix). Regardless of the dendrimer generation, no differences were observed in the g-factors of the triplet spectra. The dendrimer's contribution was negated when nanoparticle generation from iron (III) nitrate nonahydrate in methanol and water (in the absence of the dendrimer template), resulted in the same EPR signal as the dendrimer template technique. This also suggests the solvent is not directly responsible for the observed EPR signal. Obtaining an identical signal from the generation of nanoparticles from ferrocene again confirmed the dendrimer template is not responsible for the observed triplet EPR signal. The same signal was obtained when iron pentacarbonyl, $Fe(CO)_5$ in methanol was introduced (not shown), which is a known precursor of iron oxide nanoparticles in the gas phase [34], [35]. However, performing the same experiments in the absence of air or iron oxide sources resulted in no observable EPR spectral features. These experimental facts unambiguously show that the triplet spectrum was derived from Fe(III) and oxygen (*vide infra*).

E. ^{57}Fe Labeled Iron Oxide Nanoparticles

Since the oxidation of iron (III) nitrate nonahydrate in both methanol and water produced the asymmetric triplet spectra as observed with nanoparticles generated with the dendrimer technique, nanoparticles could be prepared from ^{57}Fe in the form of iron (III) nitrate nonahydrate to further access the origin of triplet spectra and conclusively show iron participates in the paramagnetic center. Theoretically the introduction of ^{57}Fe, with a non-zero nuclear spin (I=1/2), will cause a change in the magnetic field experienced by the unpaired electron and can result in hyperfine splitting. This nuclear spin will orient itself either parallel or anti-parallel with the applied magnetic field and will either add or subtract its moment from the external field. This can result in the electron resonance occurring at two distinct values that are distinguishable with sufficient resolution [36], [37]. However, often this doublet is not distinguishable and appears as broadened EPR signal [37], [38].

The resulting EPR spectra obtained after gas-phase sampling of both synthesized iron oxide nanoparticle precursors ($^{56}Fe(NO_3)_3$ and $^{57}Fe(NO_3)_3$ in water solution) are presented in Fig. 5. This synthesis route resulted in the same asymmetric triplet spectrum observed from the Zone 1 iron oxide (^{56}Fe) nanoparticles with g-factors of 2.03, 2.00, 1.96 and anisotropic shape (cf. Fig. 5, black line). However, a drastic change in spectrum was observed when ^{57}Fe doped iron (III) nitrate was used as the source of nanoparticles, Fig. 5 (red line).

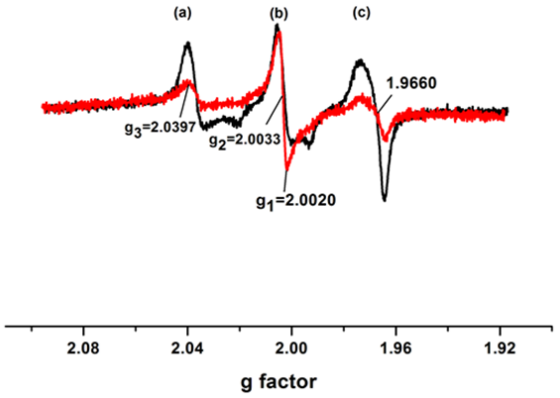

Fig. 5 Black spectrum - triplet EPR spectrum from oxidation of polypropylenimine tetra-hexacontaamine dendrimer complexed with $^{56}Fe(NO_3)_3$ nonahydrate (Zone 1). Red line – EPR spectrum generated under the same conditions but in the presence of doped ^{57}Fe as $^{57}Fe(NO_3)_3$

The reducing of chemical activity of reagents at isotope exchanges is known in the literature [39]. A similar phenomenon occurred in these experiments; not only are the total intensity of the triplet spectrum decreased (Fig. 5, red line), but also the broad, non-resolved lines (in black spectrum) between the (a) and (b) and (b) and (c) peaks are merged. Merging of peaks is typical in isotope exchange experiments [38], [39]. A broad EPR spectrum (not shown) at low yield of soot has also been detected from the experiments for soot formation in presence of ^{57}Fe doped nanoparticles (sampling from Zone 2). These data suggest Fe from iron (III) nitrate nonahydrate actively participates in the paramagnetic center and the observed triplet spectra resulted from the presence of a paramagnetic iron oxide species.

F. Role of Oxygen and the Origin of Intermediate Species from Zone 1

The same spectrum presented in Fig. 5 was obtained in all experiments using different iron (III) precursors dissolved ether in methanol or in water (rf. Figs. 2 and 7) and in presence of oxygen. This fact unambiguously indicates iron (III) and oxygen participates in the formation of the intermediate species. The large anisotropy is not similar to any organic radical containing O, N, H in a wide magnetic field window ~ 200 G. The spectrum obtained from $^{57}Fe(NO_3)_3$ in Fig. 5 at g factors g_1 = 2.0020, g_2 = 2.0033 and g_3 = 2.0397 resembles the adsorbed superoxide anion-radical ($O_2^{\bullet-}$) on metal surface site widely prevalent in the literature [40], [41].

The direct detection of $O_2^{\bullet-}$ by EPR spectroscopy is only possible if the $O_2^{\bullet-}$ is located in a lattice or bound at a solid surface [42]. Depending on the surrounding metal ion charge the g_3 (at low magnetic field) for adsorbed superoxide can be changed from 2.07 (2.08) to 2.0220 [41], [43] and is very sensitive to local environment and topography of the surface [40], [41], [44]-[46]. The three characteristic literature g-factors for the EPR spectrum of superoxide radicals are defined dominantly as an orthorhombic signal [43], [46] and are presented in Table I.

TABLE I
LITERATURE CHARACTERISTIC VALUES OF G_1, G_2 AND G_3 FOR SUPEROXIDE RADICAL ADSORBED ON DIFFERENT SURFACES

g_1	g_2	g_3	Registration temperature (K) and experimental conditions	Ref.
2.0042	2.0115	2.0340	298 K, adsorption of oxygen on a silver	52
2.0020	2.0080	2.0250	298 K, thermally, photochemically on TiO2 surfaces	53
2.0016	2.0083	2.0770	77 K, adsorption of O_2 on MgO	47
2.0033	2.0098	2.0212	77 K, interaction of H2O2 with TiAlPO-5 molecular sieve	44
2.0020	2.0090	2.0770	77K, low-temperature adsorption of oxygen on MgO	42
2.0020	2.0033	2.0397	77 K, from gas phase on Fe(III) oxide nano clusters trapped in CO2 matrix	This work
2.0016	2.066	2.113	77 K, Na-Y zeolite irradiated with γ-rays	55

The comparison of literature g-factors to our experimental data suggests that one of the superimposed spectra in Fig. 5 (red line) at g-factors $g_1 = 2.0020$, $g_2 = 2.0033$, $g_3 = 2.0397$ resembles the superoxide radical adsorbed on the surface while $g_2 = 2.0033$ differs significantly from literature values, Table I. This may be the result of very a diluted concentration of iron clusters in crystalline structure of the CO_2 matrix at 77 K or nano-sized iron nanoparticles accumulated on cold finger (*vide infra*). Note that many factors influence on EPR parameters on adsorbed superoxide on solid surfaces; for instance non-equivalency of oxygen atoms [46], [47], absorbance of superoxide on different crystalline sites (end-on adsorption) [41], ionic strength of lattice, the charge of surrounding transition metal [41], and dilution of the metal oxide in solid solution [48]. On the other hand, the anisotropic axial symmetry of superoxide with the literature values for g_{II} (= g_z =g_3) = 2.037 and $g_\perp$ (= g_x (g1) =g_y (g_2)) = 2.003 for the vanadyl ion in human hemoglobin at 77K [49] or in glassy solution of the superoxide in dipolar solvents at 77 K [50] corresponds with the data in this work (g_{II} = 2.0397 and $g_\perp$ = 2.0033).

The question then arises of how the superoxide may form on Fe (III) surfaces in the gas phase at a ~ 85˚C sampling port temperature, Fig. 1. Superoxide formation and detection predominately occurs at temperatures lower than room temperature in most cases, Table I. However, superoxides may also form at room temperature on metals [51], metal oxide surfaces (in dilute solid solutions) [48], [52], on the surface of colloidal TiO_2 [53] or on zeolite surfaces [54]. In such systems superoxides on metal oxide surfaces are stable at room temperature indefinitely. The superoxides are quickly destroyed when the samples are warmed more than 150°C [54]. The following reversible scheme for superoxide formation may account for the phenomenon observed in this work in the gas phase, (1);

$$\underset{\text{Complex 1}}{Fe(III)+O2} \leftrightarrow \underset{\text{Complex 2}}{Fe(III)\cdots O2} \leftrightarrow Fe(IV)\cdots O2 \quad (1)$$

These complexes cannot exist at high temperatures in Zone 1 (700°C); however, they may form at lower temperatures. To some extent the equilibrium (1) can be shifted to the right at cold areas in the Zone 1 (i.e. the quenching zone close to the sampling port were the temperature is ~ 85°C and after the sampling port, Fig. 1 where temperature drops drastically). The shift of equilibrium to the right (one electron reduction of oxygen to superoxide) can be dominant at time of freezing on cold finger. As a consequence, the superoxide adsorbed on highly stable Fe (IV) intermediate (Complex 2) is detected. Note that the readily accessible high oxidation state of iron is +4 [55] which is the most stable iron oxo intermediate discussed widely in many biological processes [56]-[58] and nonheme environments [57], [59]. A very dilute concentration of iron clusters (ppm level in the gas phase [1]) and their nano size advance the formation of the superoxide radical [48] and affect drastically the g_2 (the lowest value 2.0033 detected in this work on nanoparticles) and ΔH p-p (peak to peak) values of the $g_\perp$ portion of the spectrum (central line) equal 5.5 G, Fig. 5, (b) red line. The characteristic ΔHp-p values are different for superoxides adsorbed on bulk species such as 16 G (Na-Y zeolites) [54], 15.5 G (CoO-MgO solid solutions) [48], 10G (glassy aprotic solution)[50], 8G (Ba-Y zeolite) [54].

The electron transfer from Fe (III) to adsorbed oxygen, rxn 1 is similar to the natural process of one electron oxidation of Fe (II) based human hemoglobin in a biological environment [60], [61]. The occurrence of rxn 1 leads to the formation of weak signal of 3 lines always detected from different iron (III) sources in the presence of oxygen. The weakness of the spectrum is in contrast of the intense EPR signal of adsorbed superoxide radicals on transient metals produced under different types of irradiation which promotes superoxide formation yielding a good EPR signal/noise ratio (references in Table I).

To insure that the triplet spectrum is not an artifact of sampling (due to the reaction of oxygen with deposited iron oxide nanoparticles on cold finger) the experiments were repeated without Fe(III) sources, i.e. the Dewar finger, with the accumulated $Fe(III)_2O_3$ nanoclusters, was exposed to oxygen at liquid nitrogen temperature - and no triplet EPR spectrum was ever obtained.

The feature of the second constituent on spectrum Fig. 5 (red line, peak (c)) is not implicitly conclusive. The experiments with ^{57}Fe doped nanoparticles demonstrate the participation of the intermediate iron species in the formation of three asymmetric lines. Additional research is needed to clarify the nature of iron based peak (c) at g = 1.966 in Fig. 5; however, it should be noted the unidentified nature of high field EPR spectrum similar to peak (c) in superoxide detection experiments at g = 1.977 [62] and g = 1.992 [63] from the literature. Note that Fe (IV) is EPR silent and not readily detected at low CW frequencies (9.516 Ghz) at its low (S=1) or high spin (S = 2) levels [64], [65].

Therefore, due to the one electron transfer from Fe(III) to oxygen, an intermediate Fe(IV) with superoxide adsorbed on that site in the form of Fe (IV) — $O_2^{\bullet -}$ may form at quenching areas of Zone 1 in the gas-phase. This experimental fact opens future development about catalytic capability of iron containing catalysts specifically in the gas phase. The Fe (IV)

— $O_2^{\bullet -}$ intermediate formed in the cold areas on the way to the entrance of Zone 2 (Fig. 1) may easily abstract hydrogen from reagents converting to highly active iron containing peroxide by (2)

$$\text{Fe (IV) ---- } O_2^{\bullet -} + \text{RH} \rightarrow \text{Fe (IV) — O-O-H+R}\bullet \quad (2)$$

The peroxides are well known intermediate species and initiator of chain reactions due to (3)

$$\text{Fe (IV) — O-O-H} \rightarrow \text{Fe (IV) — O}\bullet + \bullet\text{OH} \quad (3)$$

Iron (IV) oxo radicals, Fe (IV)—O•, and most importantly hydroxyl radicals can enhance any chemical oxidation/pyrolysis reactions as it has been seen in soot formation processes during the oxidative pyrolysis of 1-MN [1].

IV. Conclusions

A two-zone fused silica, heterogeneous-flow reactor system was utilized to generate soot from the oxidative pyrolysis of 1-MN under atmospheric conditions in the presence of iron oxide nanoparticles. Iron oxide nanoparticles were generated from the oxidation of polypropylenimine tetra-hexacontaamine dendrimer complexed with iron (III) nitrate nonahydrate in Zone 1 of the two-zone reactor and then could impact the otherwise gas-phase reactions of 1-methylnaphthalene. Low Temperature Matrix Isolation - Electron Paramagnetic Resonance (LTMI-EPR) Spectroscopy was utilized to identify the existence of $Fe(III)_2O_3$ nanoparticles clusters with EPR fine structure characterized by g-factors of 2.00, 2.28, 3.76 and 4.37 detected on a cold finger maintained at 77 K after a multitude of experiments.

A high valence Fe(IV) reactive paramagnetic intermediate species and superoxide anion-radicals, $O_2^{\bullet -}$ adsorbed on nanoparticle surfaces in form of Fe (IV) — $O_2^{\bullet -}$ were detected from the quenching area of Zone 1 in the gas-phase. These experimental facts open future development for iron containing catalysts in the gas-phase.

Appendix

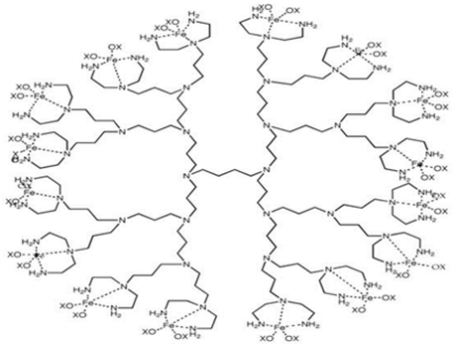

Fig. 6 Dendrimer DAB - Am32 - olypropylenimine tetra-hexacontaamine dendrimer - generation 3,4, 5 (32 amine functional groups)

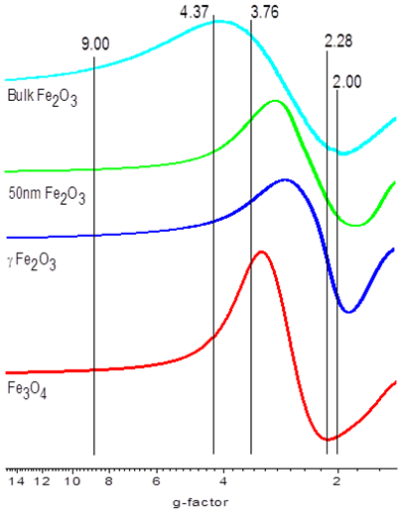

Fig. 7 EPR spectrum of iron oxide standards (10 µg transferred in 4mm EPR tube). Standards of both $Fe(III)_2O_3$ and Fe_3O_4 exhibited a large broad singlet peak with no fine structure which is typical at elevated concentrations

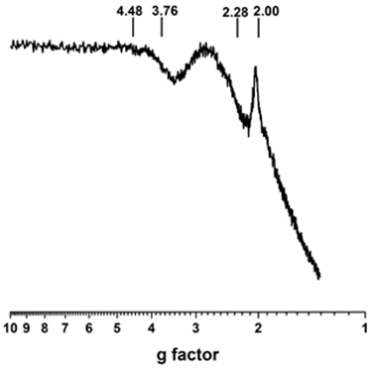

Fig. 8 After 4 months accumulation on Dewar cold-finger a barely seen peak at g = 4.37 – 4.48 has been detected

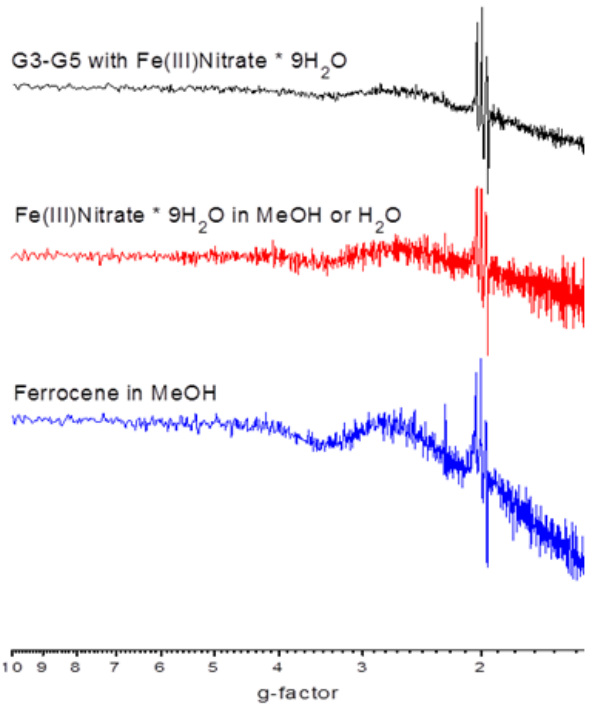

Fig. 9 EPR of intermediates generated from polypropylenimine tetra-hexacontaamine dendrimers (G3-G5 generation) complexed with iron (III) nitrate nonahydrate, iron (III) nitrate nonahydrate in methanol and water, and ferrocene in methanol

Acknowledgment

This work was partially supported by the NIEHS Superfund Research Program under grant 2 P42 ES013648-03 and the Patrick F. Taylor Chair.

References

[1] Herring MP, Potter PM, Wu H, Lomnicki S, Dellinger B. Fe2O3 nanoparticle mediated molecular growth and soot inception from the oxidative pyrolysis of 1-methylnaphthalene. Proceedings of the Combustion Institute 2013;34:1749-57.
[2] Feitelberg AS, Longwell JP, Sarofim AF. Metal enhanced soot and PAH formation. Combustion and Flame 1993;92:241-53.
[3] Hirasawa T, Sung C-J, Yang Z, Joshi A, Wang H. Effect of ferrocene addition on sooting limits in laminar premixed ethylene–oxygen–argon flames. Combustion and Flame 2004;139:288-99.
[4] Hahn DW, Kim KB, Masiello KA. Reduction of soot emissions by iron pentacarbonyl in isooctane diffusion flames. Combustion and Flame 2008;154:164-80.
[5] Ritrievi KE, Longwell JP, Sarofim AF. The Effects of Ferrocene Addition on Soot Particle Inception and Growth in Premixed Ethylene Flames. Combustion and Flame 1987;70:17-31.
[6] Linteris GT, Babushok VI. Promotion or inhibition of hydrogen-air ignition by iron-containing compounds. Proceedings of the Combustion Institute 2009;32:2535-42.
[7] Zhang J, Megaridis CM. Iron/soot interaction in a laminar ethylene nonpremixed flame. Symposium (International) on Combustion 1994;25:593-600.
[8] Kasper M, Sattler K, Siegmann K, Matter U, Siegmann HC. The influence of fuel additives on the formation of carbon during combustion. Journal of Aerosol Science 1999;30:217-25.
[9] Lomnicki S, Truong H, Vejerano E, Dellinger B. Copper oxide-based model of persistent free radical formation on combustion-derived particulate matter. Environmental Science & Technology 2008;42:4982-8.
[10] Vejerano E, Lomnicki S, Dellinger B. Formation and Stabilization of Combustion-Generated Environmentally Persistent Free Radicals on an Fe(III)2O3/Silica Surface. Environmental Science & Technology 2010;45:589-94.
[11] Dellinger B, Lomnicki S, Khachatryan L, Maskos Z, Hall RW, Adounkpe J, et al. Formation and stabilization of persistent free radicals. Proceedings of the Combustion Institute 2007;31:521-8.
[12] Nganai S, Lomnicki S, Dellinger B. Ferric Oxide Mediated Formation of PCDD/Fs from 2-Monochlorophenol. Environmental Science & Technology 2008;43:368-73.
[13] Nganai S, Lomnicki SM, Dellinger B. Formation of PCDD/Fs from the Copper Oxide-Mediated Pyrolysis and Oxidation of 1,2-Dichlorobenzene. Environmental Science & Technology 2010;45:1034-40.
[14] Khachatryan L, Adounkpe J, Maskos M, and, Dellinger B. Formation of Cyclopentadienyl Radicals from the Gas-Phase Pyrolysis of Hydroquinone, Catechol, and Phenol. Environ Sci Technol 2006; 40:5071-6.
[15] M. P. Herring, L.Khachatryan, Lomnicki S, Dellinger aB. Paramagnetic Centers in Particulate Formed from the Oxidative Pyrolysis of 1-Methylnaphthalene in the Presence of Fe(III)2O3 Nanoparticles. Comb and Flame 2013; in press.
[16] Basu P. Use of EPR Spectroscopy in Elucidating Electronic Structures of Paramagnetic Transition Metal Complexes. Journal of Chemical Education 2001; 78:666.
[17] Ledoux F, Zhilinskaya E, Bouhsina S, Courcot L, Bertho ML, Aboukais A, et al. EPR investigations of Mn2+, Fe3+ ions and carbonaceous radicals in atmospheric particulate aerosols during their transport over the eastern coast of the English Channel. Atmospheric Environment 2002; 36:939-47.
[18] Wawros A, Talik E, Zelechower M, Pastuszka JS, Skrzypek D, Ujma Z. Seasonal variation in the chemical composition and morphology of aerosol particles in the centre of Katowice, Poland. Polish Journal of Environmental Studies 2003; 12:619-27.
[19] Guskos N, Papadopoulos GJ, Likodimos V, Patapis S, Yarmis D, Przepiera A, et al. Photoacoustic, EPR and electrical conductivity investigations of three synthetic mineral pigments: hematite, goethite and magnetite. Materials Research Bulletin 2002; 37:1051-61.
[20] Gehring A, Karthein R. ESR study of Fe(III) and Cr(III) hydroxides. Naturwissenschaften 1989;76:172-3.
[21] Ibrahim MM, Edwards G, Seehra MS, Ganguly B, Huffman GP. Magnetism and Spin Dynamics of Nanoscale Feooh Particles. Journal of Applied Physics 1994;75:5873-5.
[22] Roy S, Ganguli D. Spectroscopic properties of low Fe3+-doped silica gels. Journal of Non-Crystalline Solids 1996;195:38-44.
[23] Schultz PC. Optical Absorption of the Transition Elements in Vitreous Silica. Journal of the American Ceramic Society 1974;57:309-13.
[24] Legein C, Buzare JY, Emery J, Jacoboni C. Electron-Paramagnetic-Resonance Determination of the Local-Field Distribution Acting on Cr3+ and Fe3+ in Transition-Metal Fluoride Glasses (Tmfg). Journal of Physics-Condensed Matter 1995;7:3853-62.
[25] Bishay AM, Makar L. Role of Iron in Calcium Phosphate Glasses. Journal of the American Ceramic Society 1969;52:605-&.
[26] Camara B, Oel HJ. Behavior and Effect of Iron in X-Ray-Irradiated Silicate Glass. Journal of Non-Crystalline Solids 1984;65:161-76.
[27] Baiocchi E, Montenero A, Momo F, Sotgiu A. High-Temperature Electron-Spin-Resonance Study of Fe(Iii) in Lead Silicate Glass. Journal of Non-Crystalline Solids 1980;37:143-7.
[28] Iwamoto N, Makino Y, Kasahara S. State of Fe-3+ Ion and Fe-3+--F-Interaction in Calcium Fluorosilicate Glasses. Journal of Non-Crystalline Solids 1983;55:113-24.
[29] Ledoux F, Zhilinskaya EA, Courcot D, Aboukais A, Puskaric E. EPR investigation of iron in size segregated atmospheric aerosols collected at Dunkerque, Northern France. Atmospheric Environment 2004;38:1201-10.
[30] Roy S, Ganguli D. Spectroscopic properties of low Fe3+-doped silica gels. Journal of Non-Crystalline Solids 1996;195:38-44.
[31] The Organic Chemistry of Iron. . Editors: Maitlis, PM, Stone, FGA, West, R 1978;1:257-97.
[32] Ennas G, Musinu A, Piccaluga G, Zedda D. Characterization of Iron Oxide Nanoparticles in an Fe2O3−SiO2 Composite Prepared by a Sol−Gel Method. Chemistry of Materials 1998;10:495-502.
[33] Cannas C, Gatteschi D, Musinu A, Piccaluga G, Sangregorio C. Structural and magnetic properties of Fe2O3 nanoparticles dispersed over a silica matrix. Journal of Physical Chemistry B 1998;102:7721-6.

[34] Burke NA, Stöver HD, Dawson FP. Magnetic nanocomposites: preparation and characterization of polymer-coated iron nanoparticles. Chemistry of materials 2002;14:4752-61.
[35] Huber DL. Synthesis, properties, and applications of iron nanoparticles. Small 2005;1:482-501.
[36] Baranov P, Badalyan A, Azamat D, Trepakov V, Bundakova A, Ruzanova E, et al. EPR investigation of iron-related centers in^{57} Fe-doped KTaO_ {3}. Physical Review B 2006;74:054111.
[37] Beinert H, Orme-Johnson WH. Electron-nuclear and electron-electron spin interactions in the study of enzyme structure and function Annals of the New York Academy of Sciences 1969;158:336-60.
[38] Madadi-Kahkesh S, Duin EC, Heim S, Albracht SPJ, Johnson MK, Hedderich R. A paramagnetic species with unique EPR characteristics in the active site of heterodisulfide reductase from methanogenic archaea. European Journal of Biochemistry 2001;268:2566-77.
[39] Tsibris JCM, Tsai RL, Gunsalus IC, Ormejohn.W.h., Hansen RE, Beinert H. Number of Iron Atoms in Paramagnetic Center (g = 1.94) of Reduced Putidaredoxin a Nonheme Iron Protein. Proceedings of the National Academy of Sciences of the United States of America 1968;59:959-&.
[40] Lunsford JH. ESR of Adsorbed Oxygen Species. Catalysis Reviews-Science and Engineering 1973;8:135-57.
[41] Giamello E, Sojka Z, Che M, Zecchina A. Spectroscopic Study of Superoxide Species Formed by Low-Temperature Adsorption of Oxygen onto Coo-Mgo Solid-Solutions - an Example of Synthetic Heterogeneous Oxygen Carriers. Journal of Physical Chemistry 1986;90:6084-91.
[42] Petr A, Kataev V, Buchner B. First Direct In Situ EPR Spectroelectrochemical Evidence of the Superoxide Anion Radical. Journal of Physical Chemistry B 2011;115:12036-9.
[43] Novara C, Alfayate A, Berlier G, Maurelli S, Chiesa M. The interaction of H2O2 with TiAlPO-5 molecular sieves: probing the catalytic potential of framework substituted Ti ions. Physical Chemistry Chemical Physics 2013;15:11099-105.
[44] Kanzig W, Cohen MH. Paramagnetic Resonance of Oxygen in Alkali Halides. Physical Review Letters 1959;3:509-10.
[45] Che M, Tench AJ. Non Equivalency of Oxygen Nuclei in O-17 Adsorbed on Oxides. Chemical Physics Letters 1973;18:199-202.
[46] Chiesa M, Giamello E, Paganini MC, Sojka Z, Murphy DM. Continuous wave electron paramagnetic resonance investigation of the hyperfine structure of O-17(2)- adsorbed on the MgO surface. Journal of Chemical Physics 2002;116:4266-74.
[47] Taarit YB, Lunsford JH. Electron-Paramagnetic Resonance Evidence for a Peroxy Type Superoxide Ion on Surfaces. Journal of Physical Chemistry 1973;77:780-3.
[48] Dyrek K. Chemisorption of Oxygen on Transition-Metal Oxides Studied by Epr. Advances in Molecular Relaxation Processes 1973;5:211-8.
[49] Xue DP, Lu JF, Wang K. The bidirectional effect of vanadyl ion on the oxygen affinity of human hemoglobin. Journal of Inorganic Biochemistry 1998;71:79-85.
[50] Green MR, Allen H, Hill O, Turner DR. Nature of the Superoxide Ion in Dipolar Aprotic-Solvents - Electron-Paramagnetic Resonance-Spectra of the Superoxide Ion in N,N-Dimethylformamide - Evidence for Hydrated Forms. Febs Letters 1979;103:176-80.
[51] Clarkson RB, Cirillo AC. EPR Observation of O2- Chemisorbed on a Metallic Silver Surface. Journal of Vacuum Science & Technology 1972;9:1073-&.
[52] Attwood AL, Murphy DM, Edwards JL, Egerton TA, Harrison RW. An EPR study of thermally and photochemically generated oxygen radicals on hydrated and dehydrated titania surfaces. Research on Chemical Intermediates 2003;29:449-65.
[53] Yu JH, Chen JR, Li C, Wang XS, Zhang BW, Ding HY. ESR signal of superoxide radical anion adsorbed on TiO(2) generated at room temperature. Journal of Physical Chemistry B 2004;108:2781-3.
[54] Kasai PH. Electron Spin Resonance Studies of Gamma- and X-Ray-Irradiated Zeolites. Journal of Chemical Physics 1965;43:3322-&.
[55] Harischandra DN, Zhang R, Newcomb M. Photochemical generation of a highly reactive iron-oxo intermediate. A true iron(V)-oxo species? Journal of the American Chemical Society 2005;127:13776-7.
[56] Groves JT, Haushalter RC, Nakamura M, Nemo TE, Evans BJ. High-Valent Iron-Porphyrin Complexes Related to Peroxidase and Cytochrome-P-450. Journal of the American Chemical Society 1981;103:2884-6.
[57] Krebs C, Fujimori DG, Walsh CT, Bollinger JM. Non-heme Fe(IV)-oxo intermediates. Accounts of Chemical Research 2007;40:484-92.
[58] Lacy DC, Gupta R, Stone KL, Greaves J, Ziller JW, Hendrich MP, et al. Formation, Structure, and EPR Detection of a High Spin Fe-IV-Oxo Species Derived from Either an Fe-III-Oxo or Fe-III-OH Complex. Journal of the American Chemical Society 2010;132:12188-90.
[59] Ye SF, Neese F. Nonheme oxo-iron(IV) intermediates form an oxyl radical upon approaching the C-H bond activation transition state. Proceedings of the National Academy of Sciences of the United States of America 2011;108:1228-33.
[60] Liu JG, Shimizu Y, Ohta T, Naruta Y. Formation of an End-On Ferric Peroxo Intermediate upon One-Electron Reduction of a Ferric Superoxo Heme. Journal of the American Chemical Society 2010;132:3672-+.
[61] Chung LW, Li X, Hirao H, Morokuma K. Comparative Reactivity of Ferric-Superoxo and Ferryl-Oxo Species in Heme and Non-Heme Complexes. Journal of the American Chemical Society 2011;133:20076-9.
[62] Zent AP, Ichimura AS, Quinn RC, Harding HK. The formation and stability of the superoxide radical (O(2)(-)) on rock-forming minerals: Band gaps, hydroxylation state, and implications for Mars oxidant chemistry. Journal of Geophysical Research-Planets 2008;113.
[63] Maricle DL, Hodgson WG. Reduction of Oxygen to Superoxide Anion in Aprotic Solvents. Analytical Chemistry 1965;37:1562-&.
[64] Que L. The road to non-heme oxoferryls and beyond. Accounts of Chemical Research 2007;40:493-500.
[65] Berry JF, George SD, Neese F. Electronic structure and spectroscopy of "superoxidized" iron centers in model systems: theoretical and experimental trends. Physical Chemistry Chemical Physics 2008;10:4361-74.